The GALAH survey and Gaia DR2: Linking ridges, arches and vertical waves in the kinematics of the Milky Way

Shourya Khanna,[1,2]⋆ Sanjib Sharma,[1,2] Thor Tepper-Garcia,[1,2] Joss Bland-Hawthorn,[1,2,3] Michael Hayden,[1,2] GALAH,[1,2]

[1]*Sydney Institute for Astronomy, School of Physics, A28, The University of Sydney, NSW, 2006, Australia*
[2]*ARC Centre of Excellence for All Sky Astrophysics in Three Dimensions (ASTRO-3D)*
[3]*Miller Professor, Miller Institute, UC Berkeley, Berkeley CA 94720*
[4]*Center for Astrophysical Sciences and Department of Physics and Astronomy, The Johns Hopkins University, Baltimore, MD 21218, USA*

ABSTRACT

*Gaia DR*2 has revealed substructures in the phase space distribution of stars in the Milky Way. In particular, ridge like structures can be seen in the (R, V_ϕ) plane and asymmetric arches in (V_R, V_ϕ) plane. We show that the ridges are also clearly present when the (R, V_ϕ) plane is mapped by $\langle z \rangle$ $\langle V_z \rangle$, $\langle V_R \rangle$, $\langle |z| \rangle$, [Fe/H] and [α/Fe]. The last three maps suggest that stars along the ridges lie preferentially close to the Galactic midplane ($|z| <$0.2 kpc), and, have metallicity and α elemental abundance similar to that of the Sun. We show that phase mixing of disrupting spiral arms can generate both the ridges and the asymmetric arches. It also generates discrete groupings in orbital energy, and the ridges and arches are simply surfaces of constant energy. We identify 8 distinct ridges in the *Gaia DR*2 data, six of them have constant energy while two of them have constant angular momentum. The presence of ridges in $\langle z \rangle$ and $\langle V_z \rangle$, suggests a coupling between planar and vertical directions. We demonstrate using N-body simulations, that such coupling can be generated both in isolated discs and in discs perturbed by an orbiting satellite like the Sagittarius dwarf galaxy.

Key words: Galaxy: kinematics and dynamics - stars: abundances, methods: numerical

1 INTRODUCTION

The second data release of the *Gaia* astrometric mission (DR2: Gaia Collaboration et al. 2018a) has heralded a new era in the field of Galactic Dynamics. The rich dataset provides position, parallax and proper motion ($\alpha, \delta, \omega, \mu_\alpha, \mu_\delta$) for over a billion stars at unprecedented precision (e.g., $\sigma_\mu \approx 10$ micro-arcseconds for $G <$ 14). In addition, a subset of the full dataset includes line-of-sight velocities from the *Radial Velocity Spectrometer* (*Gaia DR*2 *RVS*, Soubiran et al. 2018) for about 7 million stars, thus providing full 6D phase-space information for this sample. The sheer number of objects covered by *Gaia DR*2 combined with it's high precision, allows us to map the Galaxy's kinematics in a volume more than an order of magnitude larger than that covered by *Hipparcos* (Perryman et al. 1997). The revelation of multiple new stellar streams (Malhan et al. 2018; Price-Whelan & Bonaca 2018), evidence of non-axisymmetry through substructure in velocity (e.g., Gaia Collaboration et al. 2018b; Trick et al. 2018), etc., have all helped build a good consensus that the Galactic disc is far from being in dynamic equilibrium. Particularly remarkable was the discovery made

by Antoja et al. (2018, A18 hereafter), which revealed a spiral pattern in the (z, V_z) plane density around the Solar neighbourhood. The spiral, seen most strongly when color coded by V_ϕ, is thought to be a signature of the Galaxy relaxing from a disturbed state, through phase-mixing. Using toy models, both A18 and Binney & Schönrich (2018) suggested that the phase-spiral was evidence of the Galaxy's interaction with the Sagittarius dwarf galaxy (Sgr), and further constrain the last impact to about 0.5 Gyr ago. Recent N-body simulations (e.g., by Bland-Hawthorn et al. 2019; Laporte et al. 2018) have shown that tidal interaction with Sgr can indeed reproduce the phase-spiral seen in *Gaia DR*2, and suggest a similar timescale for the interaction. However, Khoperskov et al. (2018) have shown that the phase-spirals can also be generated through an entirely internal mechanism. In their simulations, they show that the buckling of the Galactic bar can generate bending waves in the disc. This is able to create the phase-spiral, and the wave takes about 0.5 Gyr to travel to the outer disc (10 kpc). The spirals survive well after the end of the buckling-phase, where these bending waves are supported by the disc self-gravity. These results show that it is non-trivial to distinguish between an internal or external perturbation.

A18 also revealed that the (R, V_ϕ) space has substructure in the form of diagonal ridges and that the (V_R, V_ϕ) space has arches, some

⋆ E-mail: skha2680@uni.sydney.edu.au

Table 1. Data quality cuts on *GALAH* DR2.

Selection	Comments
$9 < V_{JK} < 14$	-
$0 \leq$ Field id < 7339	Excludes data without proper selection function

of which are asymmetric about the $V_R = 0$ line. They suggest that arches are just the projection of ridges in the (V_R, V_ϕ) velocity space, however, ridges can also be present without any arches. Ramos et al. (2018) identified some of the (V_R, V_ϕ) arches and traced their median V_ϕ at different Galactocentric radius R, suggesting that arches and ridges are linked. However, a physical understanding of the connection between the ridges and arches is still missing.

Several models using various simulation techniques have been proposed to explain the ridges and arches. Most models explain either the ridges or the arches, but not necessarily both. Resonant scattering by non-axisymmetirc features rotating with a fixed pattern speed, e.g., the bar or spiral arms, has been shown to generate arches. Dehnen (2000) showed that one prominent asymmetric arch and two other weak arches can be developed by a bar, which has since been demonstrated by several other simulations (e.g., Antoja et al. 2014; Monari et al. 2017; Hunt & Bovy 2018; Hattori et al. 2019; Pérez-Villegas et al. 2017). A18 further showed that resonance with a bar can also generate ridges, but only one or possibly two ridges can be seen in the solar neighborhood as compared to the many seen in *Gaia DR*2. More recently, simulations by Fragkoudi et al. (2019) also showed that the Outer Lindblad resonance of the Galactic bar could give rise to one of the prominent ridges in the (R, V_ϕ) plane which can give rise to a Hercules-like feature in the (V_R, V_ϕ) plane.

Phase mixing models have also been used to explain these kinematic features. In such models, test particle simulations are employed. Test particles are setup to mimic a perturbation and are then evolved in a Milky Way-like potential. A18 showed that ridges can be generated using a horizontal phase mixing model, but did not show if they lead to arches. Moreover, the physical motivation for the model was also not made clear. Minchev et al. (2009) showed that phase-wrapping after interaction with a dwarf galaxy can produce multiple arches in the (V_R, V_ϕ) plane, similar to those seen in the solar neighbourhood (see also Gomez et al. 2012), but they do not explore the occurrence of ridges. This raises an interesting question: is the impact with a dwarf galaxy necessary to see multiple ridges? Quillen et al. (2018) point out that the arches seen in *Gaia DR*2 are tilted about the $V_R = 0$ line, but those generated by the phase wrapping model of Minchev et al. (2009) are symmetrical. They propose that a model in which the stars that have recently crossed spiral arms at their apocenter or pericenter can explain the asymmetric arches, however, they do not study the ridges.

Hunt et al. (2018) consider a potential with 2D transient spiral arms that wind up over time, and using the backward integration technique of Dehnen (2000), show that this perturbation can give rise to features such as the Hercules stream in the (V_R, V_ϕ) plane, as well as multiple ridges in the (R, V_ϕ) plane, and multiple asymmetric arches. Transient spiral arms have been shown to develop in self gravitating disc simulations (Sellwood 2011). This sets up the motivation to look for ridges and arches in self gravitating disc N-body simulations. Quillen et al. (2011) showed that asymmetric arches can be generated in self gravitating N-body simulations, but did not study the ridges in (R, V_ϕ). Laporte et al. (2018) studied N-body simulations involving interaction with a dwarf galaxy, and

were able to generate ridges in (R, V_ϕ), but only one arch or moving group could be seen in the (V_R, V_ϕ) plane. An interesting question to ask is whether the source of the ridges and arches is internal or external, and how we could distinguish between the two. Can a phase mixing model motivated by transient spiral arms explain multiple ridges and multiple asymmetrical arches?

Vertical waves have also been reported in the *Gaia DR*2 data (e.g., Gaia Collaboration et al. 2018b; Bennett & Bovy 2019). Already with the limited coverage of *Gaia-TGAS*, Schönrich & Dehnen (2018) and Huang et al. (2018) found that the vertical velocity in the solar neighborhood varies with angular momentum J_ϕ. They found a large scale trend of V_z increasing monotonically with J_ϕ, which is the signature of the Galactic warp. Superimposed on this large scale trend, they also found undulations, indicative of a wave like pattern. Undulations in the profile of V_z as function of Galactocentric radius R were also reported by Kawata et al. (2018). Gómez et al. (2013) and D'Onghia et al. (2016) both show that undulations in the $V_z(R)$ profile can be seen in N-body simulations involving interaction with Sgr. However, variation of V_z as a function of angular momentum was not studied. Are these vertical waves linked to ridges and arches? Can these vertical waves be seen in simulations with or without the interaction of Sgr? This is a question we attempt to address.

In this paper, we revisit the (R, V_ϕ) ridges seen in *Gaia DR*2. First, we study and characterize the ridges. We dissect the ridges using radial velocity, vertical height, and vertical velocity. Furthermore, we also explore the nature of ridge stars by considering elemental abundances from *GALAH*, and relate this to the nature of the perturbation itself. Next, we simulate phase mixing of spiral arms and show how this model can be used to understand the connection between the (R, V_ϕ) ridges and the (V_R, V_ϕ) arches. Finally, we carry out N-body simulations of the galactic disc both with a Sgr-like perturber and without any perturber and study the phase-space features in these simulations and compare them with those seen in *Gaia DR*2.

2   DATASET AND METHODS

Throughout the paper we adopt a right handed coordinate frame in which the Sun is at a distance of $R_\odot = 8.2$ kpc from the Galactic center (Bland-Hawthorn & Gerhard 2016), consistent with the new ESO Gravity measurement (Gravity Collaboration et al. 2018), and has Galactocentric coordinates $(X, Y, Z) = (-8.2, 0, 0.25)$ kpc. The cylindrical coordinate angle $\phi = \tan^{-1}(Y/X)$ increases in the anti-clockwise direction, while the rotation of the Galaxy is clockwise. The heliocentric Cartesian frame is related to Galactocentric by $X_{hc} = X + R_\odot$, $Y_{hc} = Y$ and $Z_{hc} = Z$. X_{hc} is negative toward $\ell = 180°$ and Y_{hc} is positive towards Galactic rotation. For transforming velocities between heliocentric and Galactocentric frames we use $(\dot{X}_\odot, \dot{Y}_\odot, \dot{Z}_\odot) = (U_\odot, \Omega_\odot R_\odot, W_\odot)$. Following Schönrich et al. (2010), we adopt $(U, V, W)_\odot = (11.1, 12.24, 7.25)$ km s^{-1}, while for the azimuthal component we use the constraint of $\Omega_\odot = 30.24$ km s^{-1}kpc^{-1} which is set by the proper motion of Sgr A*, i.e., the Sun's angular velocity around the Galactic center (Reid & Brunthaler 2004). This sets the rotation velocity at the Sun to $V_{\phi,\odot} = -248$ km s^{-1}, and thus the circular velocity at the Sun to $V_{c,\odot} = -236$ km s^{-1}. We now describe the astrometric and spectroscopic data that we use in this work and the quality cuts that we apply on them.

Table 2. Parameters for the isolated Galaxy (Model P). Column headers are as follows: M_t := total mass (10^9 $M_\odot$); r_s := scalelength (kpc); r_{tr} := truncation radius (kpc); N_p := number of particles (10^6).

	Profile	M_t	r_s	r_{tr}	N_p
Galaxy					
DM halo	H	10^3	38.4	250	10
Bulge	H	9	0.7	4	1
Thick disc	MN	20	5.0^a	20	2
Thin disc	Exp/Sech	28	5.0^b	20	3

Notes. H := Hernquist (1990) profile; MN := Miyamoto & Nagai (1975) profile; Exp := radial exponential profile.; Sech := vertical $sech^2z$ profile.
^{a} scaleheight set to 0.5 kpc.
^{b} scaleheight set to 0.3 kpc.

Table 3. N-body models and properties of the perturber . Column headers are as follows– M_{tot}: total mass (10^9 $M_\odot$); M_{tid} : tidal mass (10^9 $M_\odot$); r_{tr} : truncation radius of dark matter in kpc; N_p : number of particles (10^5 and v_0: approximate initial orbital speed in km s^{-1}. See the notes below the table for more information.

Model	M_{tot}	M_{tid}	r_{tr}	N_p	v_0
P (unperturbed/isolated galaxy)	0				
S (intermed. mass, one transit)	50	30	19	1	360
R (high mass, one transit)	100	60	24	2	372

Notes. Both the DM halo and the stellar component are initially modelled as Hernquist spheres with r_s = 9.8 kpc and r_s = 0.85 kpc, respectively. The mass of the stellar component is 4×10^8 $M_\odot$ in either case, split among 4×10^4 particles.

2.1 Gaia DR2 RVS sample

In this paper we make use of the *Gaia DR*2 radial velocity sample (*Gaia DR*2 *RVS*) which provides full 6D phase space information ($\alpha, \delta, \omega, \mu_\alpha, \mu_\delta, V_{los}$). We selected stars with positive parallax and with parallax precision $\sigma_\omega/\omega < 0.2$, which gave a sample of 6376803 stars. The SQL query used to generate the sample is given in section A. We estimated distance as $1/\omega$, which is reasonably accurate for our selected stars and for the purpose of this paper.

2.2 GALAH DR2 sample with elemental abundances

The spectroscopic data used here is taken from an internal release of *GALAH* DR2, which includes, public data (Buder et al. 2018, DR2), and fields observed as part of the *K2-HERMES* (Wittenmyer et al. 2018) and *TESS-HERMES* (Sharma et al. 2018) programs. To maintain the survey selection function, we have applied the quality cuts summarised in Table 1, which gives a total of 465870 stars crossmatched with *Gaia DR2*. This internal release includes non-LTE corrections on [Fe/H] but not on [α/Fe]. For the kinematics of this dataset, we make use of the parallax and proper motion ($\omega, \mu_\alpha, \mu_\delta$) from *Gaia DR2*, but use the highly precise radial velocities from *GALAH*, which have typical error of 0.1 km s^{-1} (Zwitter et al. 2018). Since we are mainly interested in nearby stars, we restrict our *GALAH* sample only to dwarfs, by applying a surface gravity cut of (log $g > 3$), which results in a final sample of 258289 stars. This avoids any issues related to systematic errors in stellar parameters between dwarfs and giants.

2.3 Phase mixing simulations

To understand the origin of the phase space substructures like ridges and arches, we perform simulations in which spiral arms phase mix and disrupt over time. The simulations are motivated by the desire to mimic the effect of transient spiral arms. For this we consider an initial distribution of particles confined to four thin spiral arms. The radial distribution was assumed to be skew normal with skewness of 10, location parameter of 4 and scale parameter of 6. The radial velocity was sampled from $\mathcal{N}(0, 20)$ and azimuthal velocity from $\mathcal{N}(\Theta(R), 20)$, where $\Theta(R)$ denotes the circular velocity. For simplicity the particles were set up in the mid plane with zero vertical velocity. A total of 640,000 particles were evolved for 650 Myr with galpy (Bovy 2015) using the MWPotential2014 potential, consisting of an axis-symmetric disc, a spherical bulge and a spherical halo. The setup is similar to (Antoja et al. 2018), but they start with stars arranged in a single line as compared to four spiral arms used by us.

2.4 N-body simulations

Another approach that we adopt, in order to gain insight into the origin of phase space substructures, is the use of N-body simulations of a full multi-component Galaxy. Ideally, we would like to carry on a detailed modelling of every component of the Galaxy, both collisionless (e.g. dark matter and stars) and gas. This is, however, not feasible as it is both computationally expensive and non-trivial to do. We adopt a common, simplifying assumption: we assume that a pure N-body (rather than a full N-body, hydrodynamical) model is sufficient for our purposes. We caution that neglecting the gas components in these type of experiments may not always be appropriate (see e.g. Tepper-García & Bland-Hawthorn 2018).

We consider here the following two scenarios as the plausible origin of the ridges: i) instabilities internal to the Galaxy; and ii) tidal (external) interactions. In consequence, we focus our attention on one representative model for each of these. On the one hand, we simulate the evolution of an isolated Galaxy starting from some prescribed initial conditions (see below). On the other hand, we simulate how the stars behave in a Galaxy that has been tidally perturbed by the interaction with a smaller system. It has been suggested that Sgr may lie behind many of the kinematic features revealed by *Gaia DR*2 (e.g. Antoja et al. 2018; Binney & Schönrich 2018; Laporte et al. 2018; Bland-Hawthorn et al. 2019). It therefore seems natural in our case to simulate the interaction of the Galaxy with a Sgr-like perturber.

Our isolated model Galaxy consists of four collisionless components: a host DM halo; a stellar bulge; a thick stellar disc; and a thin stellar disc. We refer to this model as the 'isolated' model (Model P). See Table 2 for details of this model Galaxy. Note that the values for structural parameters (scalelength, scaleheight, etc.) are only broadly consistent with the range of values inferred from observations (Bland-Hawthorn & Gerhard 2016). That said, we note that these differences does not affect in any significant way our results.

Our interaction models consist essentially of a two-component (DM, stellar spheroid) system orbiting an initially isolated Galaxy along an (unrealistic) hyperbolic orbit. The reason for choosing such an orbit rather than a more realistic orbit for the perturber is that, as we have shown previously (Bland-Hawthorn et al. 2019), each passage of Sgr across the Galactic plane washes out the kinematic signatures of its previous crossing, thus limiting the time span available between crossings. In contrast, by adopting a hyperbolic orbit
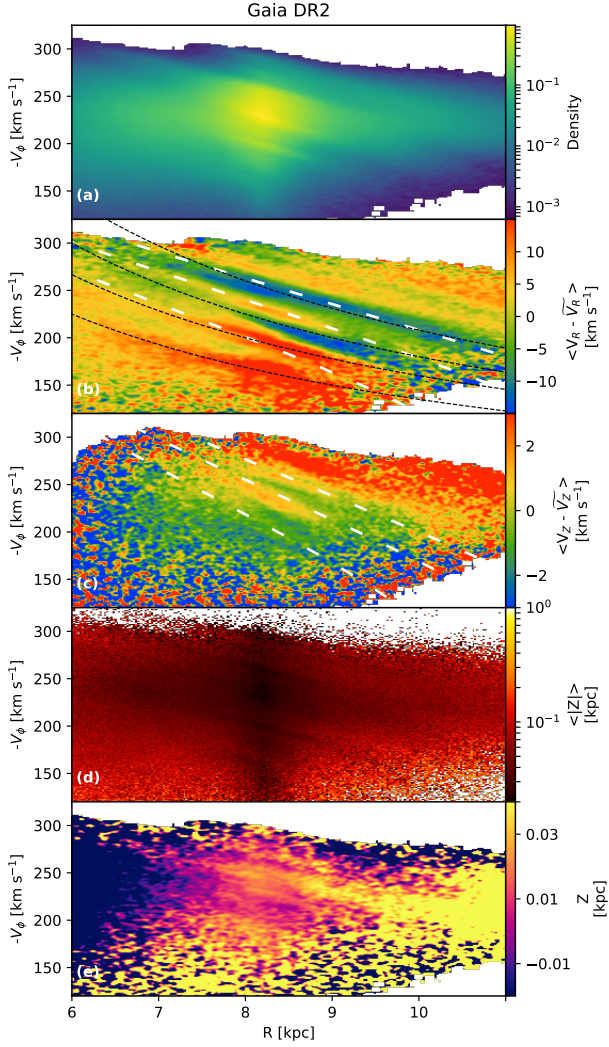
Figure 1. Study of the (R, V_ϕ) plane with *Gaia DR*2 RVS. We select stars in the region $(|\phi - 180°| < 25°)$ & $(|R - R_\odot|/\text{kpc} < 3.5)$. Heat maps of various quantities are shown; a) probability density of V_ϕ conditional on R $(p(V_\phi|R))$ b) mean radial motion $\langle V_R \rangle$ c) mean vertical motion $\langle V_z \rangle$ d) mean absolute distance from the plane $|z|$ and e) distance from the plane z. The white dotted curves represent constant energy for values of -0.112, -0.021, & 0.097 for $(E - E_{\text{circ}}(R_\odot))/V_{\text{circ}}^2(R_\odot)$. Black curves represent constant angular momentum, $L_z = (1350, 1600, 1800, 2080)$ kpc km s^{-1}.

we ensure that Sgr transtis the Galactic plane (disc) once only, thus facilitating the analysis of its effect on the Galactic stars.

We consider perturbers with total masses of 5 or $10 \times 10^{10}\,M_\odot$, spanning the mid-to-high range of plausible Sgr masses at infall (e.g Niederste-Ostholt et al. 2010). Both the stellar system and the dark halo are modelled as truncated Hernquist (1990) spheres. Their scale radii are initially set at 0.85 and 10 kpc, respectively. The stellar system is initially truncated at 2.5 kpc while the truncation radius of the dark halo is listed in Table 3. A simulation with each of these masses was started with the perturber at $(x, y, z) = 20.8, 0., 45.5)$ kpc on an orbit of eccentricity $e = 1.3$ (hyperbolic) and pericentric distance 10 kpc.[1]

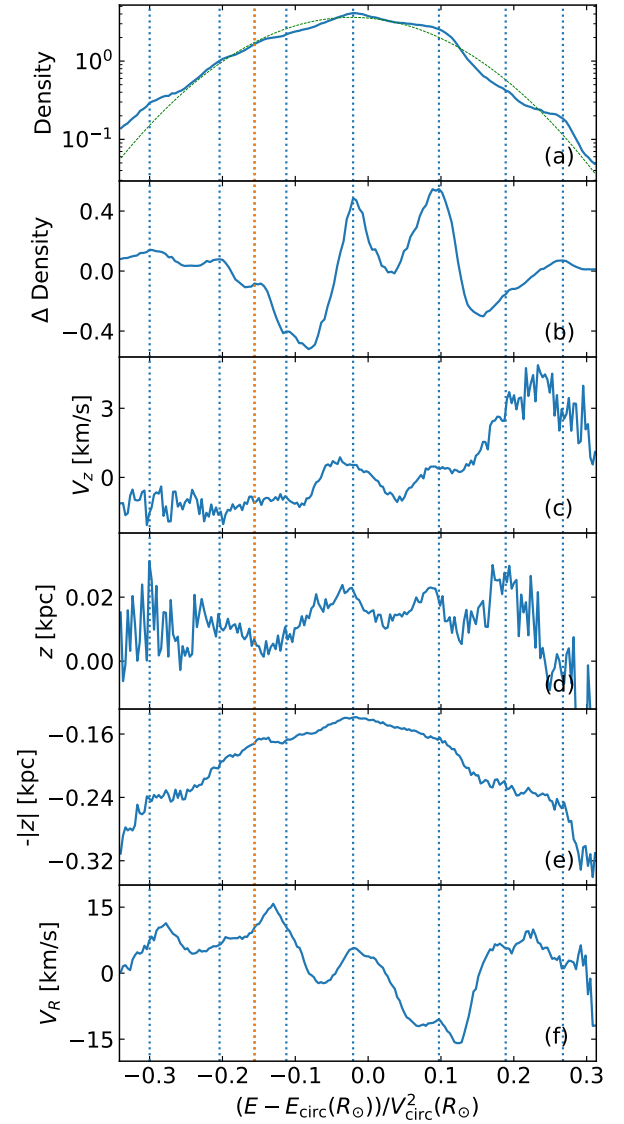[1] The exact inital initial velocities for model R and model S was

Figure 2. Profiles of different quantities as a function of energy for stars in $(|R - R_\odot| < 1.0)$&$(|\phi - \phi_\odot| < 25)$. a) Density distribution along with best fit skewed normal distribution (green line). b) Residual of density after subtracting a skewed normal distribution. c) Median vertical velocity d) Median vertical distance above the plane. e) Median absolute value of distance from the plane. f) Radial velocity. The peaks are located at $[-0.300, -0.204, -0.156, -0.112, -0.021, 0.097, 0.189, 0.267]$. The peaks are approximately regularly spaced with mean separation of 0.095, except for the peak at -0.0156 corresponding to the Hercules stream.

Two key requirements on these type of simulations, imposed by the exquisite detail on the kinematics of stars revealed by the data, are the mass resolution (or particle number) and the limiting spatial resolution. The latter has to be low enough to allow for a correct simulation of the evolution of the dynamically coldest stellar component within $|z| < 0.2$ kpc. The former needs to be high enough to allow for a dense enough sampling of the (R, V_ϕ).

$(v_x, v_y, v_z) = (-267, 0., -260)$ km s^{-1} and $(v_x, v_y, v_z) = (-258, 0., -251)$ km s^{-1}, respectively.
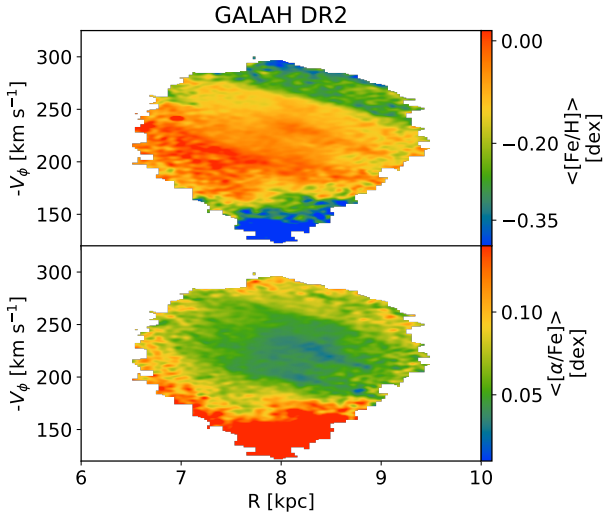
Figure 3. Study of the (R, V_ϕ) plane with elemental abundances from *GALAH* DR2 for stars in ($|R - R_\odot|/kpc < 3.5$)&($|\phi - \phi_\odot| < 25$). (a) [Fe/H] map. (b) [α/Fe] map. Ridges are comprised of metal rich and alpha-poor stars.

We choose values for the particle number and spatial resolution such that we fulfill these requirements while keeping the computational cost of the simulations reasonably low. More specifically, we set the limiting spatial resolution at 30 pc, to be compared with 300 pc, the (initial) scaleheight of the cold stellar disc, which is the smallest length scale in our simulation. The adopted particle number varies from component to component, depending on the total mass of the component and the corresponding particle mass; as per our above discussion, the thick stellar disc and the thin stellar discs have been assigned the absolute highest particle number (see Table 2).

The simulations' axisymmetric initial conditions, i.e. the particles' positions and velocities for each component were assigned by the technique of Springel et al. (2005) as implemented in the DICE code (Perret et al. 2014). In doing so, all the components are intended to be in dynamical equilibrium with the total potential of the compound system. However, in reality they will in general be slightly out of equilibrium (e.g. Kazantzidis et al. 2004), and even an isolated Galaxy the disc will develop some small-scale structure, such as rings and transient spirals. While usually an unwanted numerical artifact in experiments like ours, here we actually need these instabilities in order to investigate their effect on the stellar phase-space kinematics. In real galaxies, such transient features will develop as well, but for reasons yet to be fully understood.

The evolution of the system[2] in each case is calculated with the adaptive mesh refinement (AMR) gravito-hydrodynamics code RAMSES (version 3.0 of the code described by Teyssier 2002). Simulation data is dumped to disc at approximately $\Delta\tau = 10$ Myr intervals. A set of movies showing the evolution of the system in each model are provided at Gaia-GALAH-phase-spiral.

3 RESULTS

We begin by studying the (R, V_ϕ) plane using the observed data. Next we compare the observed results with predictions from two type of simulations, phase mixing simulation of disrupting spirals and disc N-body simulations. This is followed by a study of the (V_R, V_ϕ) plane and subsequently the (V_R, R) plane. In both cases we compare the observed results with the predictions from the simulations.

3.1 Analysis of the (R, V_ϕ) plane using the observed data

3.1.1 Dissection in Kinematics and vertical height with Gaia

Antoja et al. (2018) revealed the diagonal ridge like structures in the (R, V_ϕ) density distribution. In this section, we further explore this plane using kinematics and vertical height. In Figure 1, we show results using the *Gaia DR2 RVS* sample. We select stars with ($|\phi - 180°| < 25°$) & ($|R - R_\odot|$/kpc < 3.5).

Figure 1a), shows the density distribution. Multiple diagonal ridges are clearly visible, extending between $6 < R/\text{kpc} < 12$. Ridges are prominent at $R = 8.2$ kpc, but seem to fade away as we move away from the solar radius, this is because, as we move away from the Sun there is a fall in number density of stars and an increase in uncertainty in R and V_ϕ. Figure 1b, shows a map $\langle V_R \rangle$ in (R, V_ϕ) plane. Th ridges are more prominent and are visible even at large distances from the solar neighborhood. They appear at similar location to that in the density map in Figure 1a). Stars along the ridges are moving, either radially outward or inward, with respect to the background distribution, with $\langle V_R \rangle \approx 10$ km s^{-1}.

Next we explore the properties of the ridges in the vertical direction. Figure 1c, shows a map of $\langle V_z \rangle$ in the (R, V_ϕ) plane. The ridge structure can again be seem but is weaker as compared to the $\langle V_R \rangle$ map. Three ridges are clearly visible and the $\langle V_z \rangle$ associated with the structures is about 2 km s^{-1}. Figure 1d shows (R, V_ϕ) mapped by $|z|$, i.e., distance from the mid-plane of the disc. The ridges are primarily composed of stars that lie close to the Galactic plane ($|z| \lesssim 0.2$ kpc), as indicated by the distinctive dark color. It is important to note, that if stars at all heights above the plane participated in the ridges, the $|z|$ map in Figure 1d would be completely featureless. This preferential distribution must thus be linked to the nature of the perturber responsible for the ridges. Three ridges are also visible in the map of z, the distance from the plane (Figure 1e).

We have over-plotted curves of constant angular momentum (black dotted lines) at $L_z = [1350, 1600, 1800, 2080]$ kpc km s^{-1}, and curves of constant orbital energy E (white dashed lines) at $(E - E_{\text{circ}}(R_\odot))/V^2_{\text{circ}}(R_\odot) = [-0.112, -0.021, 0.097]$. Energy was evaluated using the MWPotential2014 potential in galpy (Bovy 2015). Both the curves decrease with R and resemble like ridges, and hence either of them can be used to label the ridges. The difference between the two is that the constant energy curves are straight lines but angular momentum ones are not. From these plots it is difficult to say if the ridges are constant energy or constant angular momentum, we revisit this issue later in subsection 3.2.

We have shown that the ridges are present in maps of density, kinematics and vertical height. We now investigate if the the ridges in the maps of different quantities are correlated with each other. For this we select stars in a narrow range in R and then study the one dimensional profiles of various quantities as a function of orbital energy E (Figure 2). We choose E instead of V_ϕ, as ridges are well approximated by curves of constant energy. We use the MWPotential2014 potential in galpy to compute the energy (Bovy 2015). Instead of directly using E, we use the dimensionless form
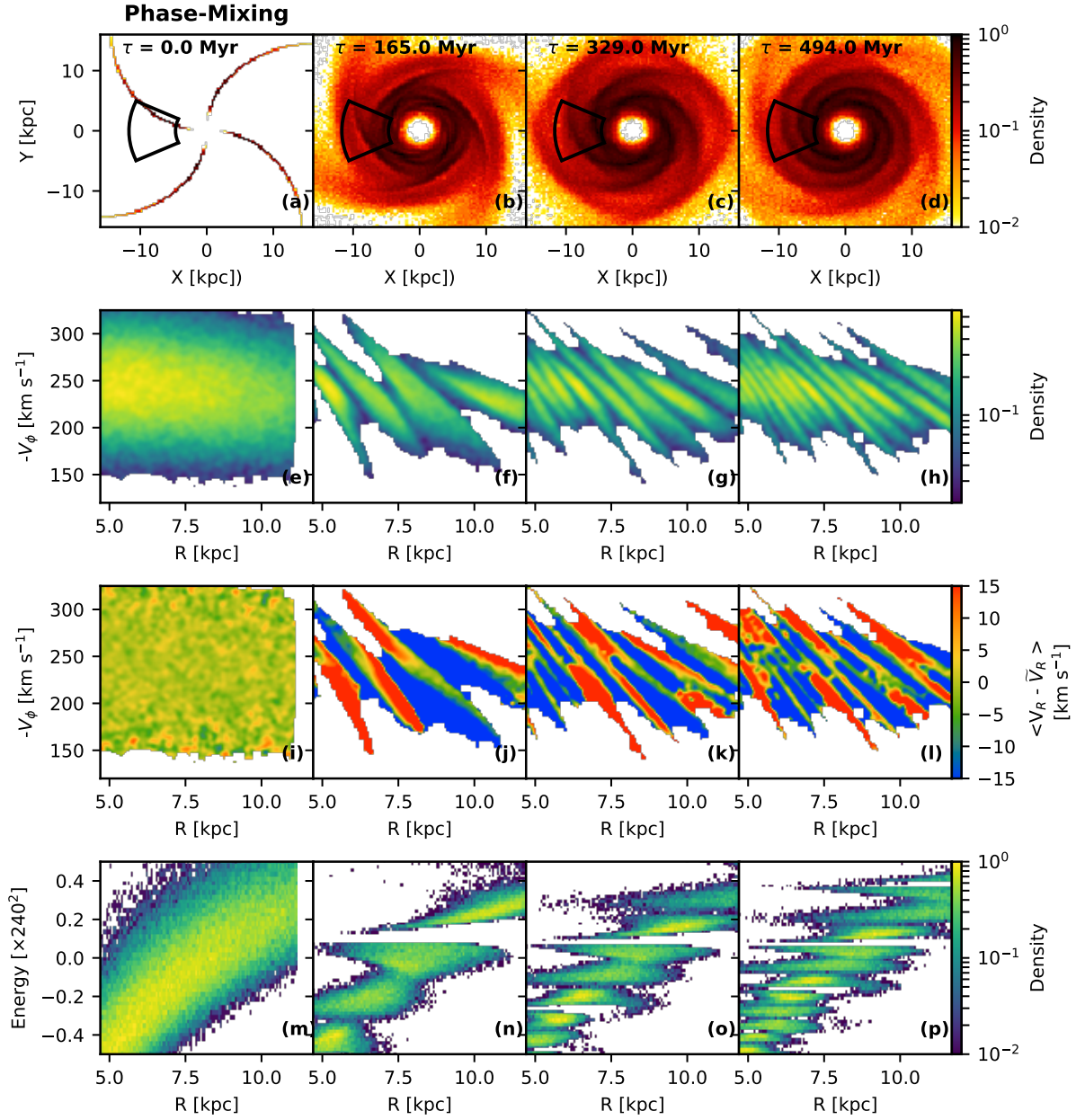
Figure 4. Evolution of stars in the phase mixing simulation (subsection 2.3). Panels(a-d) show the density in xy plane for five different time snapshots. Panels(e-h) show the (R, V_ϕ) plane mapped by density. Panels(i-l) show the (R, V_ϕ) plane mapped by $\langle V_R \rangle$. Panels (m-p) show the total energy against R. For panels(e-p), stars are selected in $(|R - R_\odot| < 5.0)\&(|\phi - \phi_\odot| < 25)$, indicated by the locus in Panel a.

given by $E' = (E - E_{\text{circ}}(R_\odot))/V^2_{\text{circ}}(R_\odot)$, where V_{circ} is the circular velocity at a given radius, and E_{circ} is the energy of a star in a circular orbit at $(R, z) = (R_\odot, 0)$. Figure 2(a,b) show the density profiles. At least 8 peaks can be identified and these are marked with vertical dotted lines. The peak at $E' = 0.156$ corresponds to the Hercules stream and is shown with a different color. Figure 2(c) shows the profile of mean vertical velocity. A large scale trend of increase in V_z with E can be seen similar to Schönrich & Dehnen (2018) who studied V_z as a function of L. Note, for a given R and V_R, E increases monotonically with L, and here the range of R is almost constant and V_R is small. This large scale trend of V_z is due to warp. Besides the large scale trend, peaks at $E' = [-0.021, 0.097]$ can also be seen. The location of these peaks matches with peaks

seen in density. Figure 2(d) plots median vertical distance z. There is no large scale trend, but 3 peaks ($E' = [-0.21, 0.097, 0.189]$) are clearly identifiable and they match with the peaks in density. Two of the peaks also match with peaks in V_z. Figure 2(e) shows the median value of $-|z|$. Almost all density peaks have a corresponding peak in this plot, which is a reflection of the fact that the stars in the density peaks lie close to the Galactic plane. Finally, Figure 2(f) shows the profile of median V_R. Although all peaks do not match in location with all peaks in density, however, for each undulation in the profile of density there is an undulation in V_R. This suggests that V_R and density peaks are strongly correlated with each other. Note, a consequence of V_R peaks not matching up with density peaks is
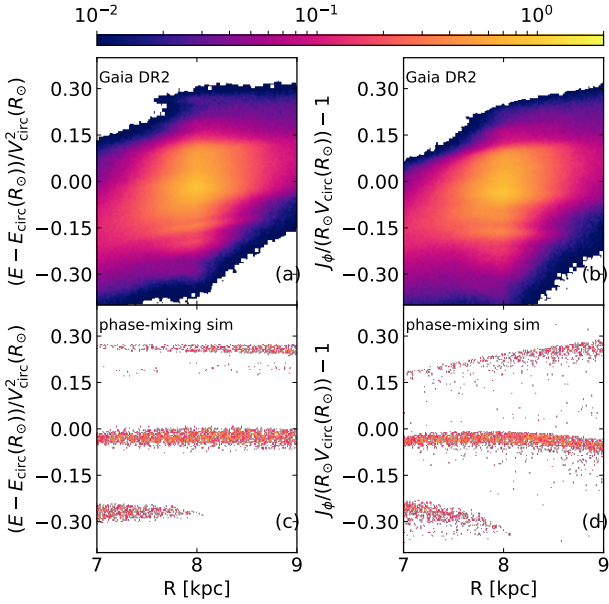
Figure 5. Energy E and angular momentum J_ϕ as a function of Galacto-centric radius R. a) Gaia DR2. b) Phase mixing simulation of a single spiral arm after an evolution of $\tau = 650$ Myr.

that stars in a ridge are not symmetrically distributed about V_R, and arches in (V_R, V_ϕ) plane show such a behaviour.

3.1.2 Dissection in elemental abundances with GALAH

We now study the elemental abundance in the (R, V_ϕ) plane. In Figure 3a, (R, V_ϕ) is mapped by [Fe/H]. For the region $200 < V_\phi < 250$ the background metallicity is around [Fe/H]≈ -0.1, reflecting the local ISM around the solar neighbourhood which is sub-solar (Nieva & Przybilla 2012). The ridges in this region however, are mainly composed of solar metallicity stars, with typical [Fe/H]≈ 0.03. In Figure 3b (R, V_ϕ) is mapped by [α/Fe]. The ridges stand out as a population with [α/Fe]≈ 0.05 (close to solar values). This is consistent with ridges being made of stars that lie predominantly in the plane. Stars close to the plane are younger and young stars are metal rich and alpha-poor (age-scale-height and age-metallicity relations, e.g., Mackereth et al. 2017).

Beyond $L_Z = 2080$ (top-most white dotted curve) there is a sharp cut-off in metallicity (Figure 3c). This region is dominated by relatively metal-poor stars with typical [Fe/H]≈ -0.3, and is also alpha-enhanced around [α/Fe]≈ 0.1 (Figure 3d). This suggests that the origin of these stars is different from those along the ridges. $L_Z > 2080$ corresponds to a guiding radius $R_G > 9.5$ kpc (assuming a flat rotation curve). These stars thus belong to the outer disc and their low metallicity is consistent with the Galaxy's negative metallicity gradient with R (Hayden et al. 2014).

Similarly, stars at the bottom of Figure 3(a,b) with $V_\phi < 150$ also show a sharp change in abundances. These stars have large asymmetric drift, are rotating slowly, have [α/Fe]> 0.14 and [Fe/H]< -0.4. These properties are consistent with that of the traditional thick disc, which is metal-poor and alpha-enhanced and kinematically hot (Bensby et al. 2014; Duong et al. 2018, etc.).

3.2 Analysis of the (R, V_ϕ) plane using phase-mixing simulation

We now consider a toy model of phase mixing similar to that used by (Antoja et al. 2018) to explain some of the features seen in (R, V_ϕ) plane. We consider an initial distribution of particles confined to four thin spiral arms, in (Antoja et al. 2018) the particles were confined to a single line. The particles are then evolved in time under a multi-component analytic potential. The simulation is designed to mimic phase mixing of pertirbations caused by transient spiral arms (for further details see subsection 2.3).

The distribution of stars in the (X, Y) and the (R, V_ϕ) planes are shown in Figure 4 for four different time snapshots. Also shown are maps of $\langle V_R \rangle$ in the (R, V_ϕ) plane. As we move forward in time the spiral pattern decays and the ridges start to form and they increase in number and become more and more thinner. The ridges can also be seen in maps of V_R. The ridges are approximately linear in the (R, V_ϕ) plane and resemble lines of constant angular momentum. The appearance of the ridge structure is a consequence of phase mixing and can be understood in terms of the *Liouville*'s theorem , which states that the full phase space density of a system evolving in a fixed potential is conserved. In the case of our simulation, the phase space is made of (X, Y, V_X, V_Y). Initially the density in the (X, Y) space is high while that in (V_R, V_ϕ) space is low. As the spiral pattern disperses the density in the (X, Y) plane reduces, but to conserve the phase space density the density should increase in other dimensions. The structures in the (R, V_ϕ) are a reflection of this phenomena.

The bottom panels show the distribution of stars in the plane of orbital energy and Galacto-centric radius, (E, R) plane. Discrete energy levels can be seen. Stars in a ridge lie in a narrow energy interval. We explore this further in Figure 5. The figure shows the distribution of stars in the (E, R) and (J_ϕ, R) plane. The top panels show results for *Gaia DR2*, while the bottom panels are for phase mixing simulation. For the simulation we only show stars belonging to a single spiral. It is clear from Figure 5(c,d) that in phase mixing simulations, the ridges are curves of constant energy rather than constant angular momentum. For the observed data, ridges between $-0.15 < E' < 0$ look flat in J_ϕ, while the rest of the ridges, specially with large values of $|E|'$ look flat in E'.

3.3 Analysis of the (R, V_ϕ) plane using disc N-body simulations

We now consider the more realistic N-body simulations of the Galaxy, described in subsection 2.4. The first scenario, Model P, is that of an isolated galaxy, i.e., unperturbed by a satellite. The (X, Y) density of four selected snapshots at $\tau = [0.21, 0.56, 0.97, 2.59]$ Gyr are shown in Figure 6(a-d). At $\tau = 0.21$ Gyr (Figure 6a), the disc settles into an equilibrium configuration and develops tightly wound spiral arms. Such self-excited instabilities forming spiral arms are a known feature of N-body simulations in disc galaxies (Sellwood 2012). The corresponding (R, V_ϕ) density map (Figure 6e), is largely uniform and lacks ridge like substructure as seen in *Gaia DR2* (in Figure 1). Similarly, in the velocity maps (Figure 6(i,m)), there are blobs in kinematics with $\langle V_R \rangle \approx 10$ km s^{-1} and $\langle V_z \rangle \approx 3$ km s^{-1}, but no ridges can be seen.

By $\tau = 0.56$ Gyr, the spiral arms have weakened slightly, they are fewer and thicker(Figure 6b). Interestingly, the (R, V_ϕ) density at this snapshot shows large scale diagonal stratification, with a span of about 4 kpc (Figure 6f). The $\langle V_R \rangle$ map shows multiple thin
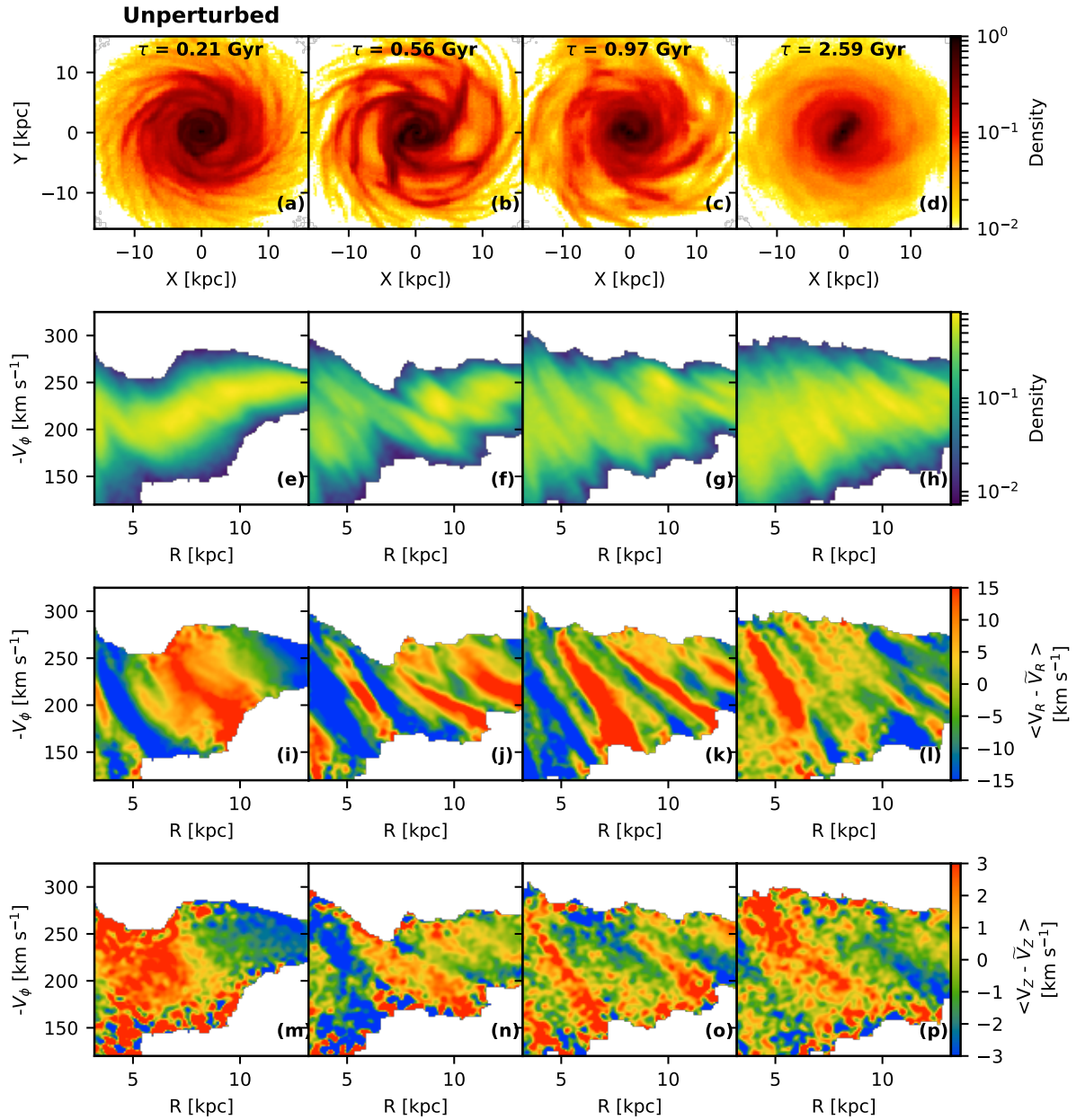
Figure 6. Evolution of stars in the N-body simulation of an unperturbed disc (Model P). Panels(a-d) show the density in xy plane for four different snapshots at $\tau = [0.21, 0.56, 0.97, 2.59]$ Gyr. Panels(e-f) show the (R, V_ϕ) plane mapped by density. Panels(i-l) show the (R, V_ϕ) plane mapped by $\langle V_R \rangle$. Panels(m-p) show the (V_R, V_ϕ) plane mapped by $\langle V_z \rangle$. In Panels(e-p), stars are selected in the region $(|R - R_\odot| < 5.0)\&(|\phi - \phi_\odot| < 25)$.

diagonal ridges with alternating pattern of radially outward and inward motion (Figure 6(j)).

By the next snapshot at $\tau = 0.97$ Gyr, the spiral arms are found to have diffused and weakened (Figure 6c). The corresponding (R, V_ϕ) density map shows several prominent ridges that extend over $5 < R/kpc < 15$ and have a more linear appearance compared to the previous snapshot (Figure 6g). The ridges are also clearly present in the $\langle V_R \rangle$ and $\langle V_z \rangle$ maps, where the amplitude of the radial oscillations is again higher than the vertical component.

By the final snapshot, chosen at $\tau = 2.59$ Gyr, the spiral arms are found to have significantly decayed. A central bar with half-length of ~ 2.5 kpc is visible prominently (Figure 6d). The density, $\langle V_R \rangle$ and $\langle V_z \rangle$ maps continue to show large scale ridges

(Figure 6(h,i,p)). In summary, Figure 6 shows that an unperturbed galaxy can reproduce ridges in the (R, V_ϕ) plane with features similar to that seen in *Gaia DR*2. The ridges appear as the spiral structure decays, and are maintained as long as this decay is going on. As was already mentioned in subsection 3.2, this is a consequence of *Liouville*'s theorem which requires that the full density in phase-space is always conserved. This suggests that internal instabilities such as transient spiral arms, could be responsible for the ridges seen in Figure 1.

Next, we consider the scenario where the Galaxy is tidally perturbed by an orbiting satellite. Model S simulates the interaction with an intermediate mass Sgr galaxy ($5 \times 10^{10} M_\odot$), while Model R simulates the interaction with a heavier Sgr galaxy ($10^{11} M_\odot$). In
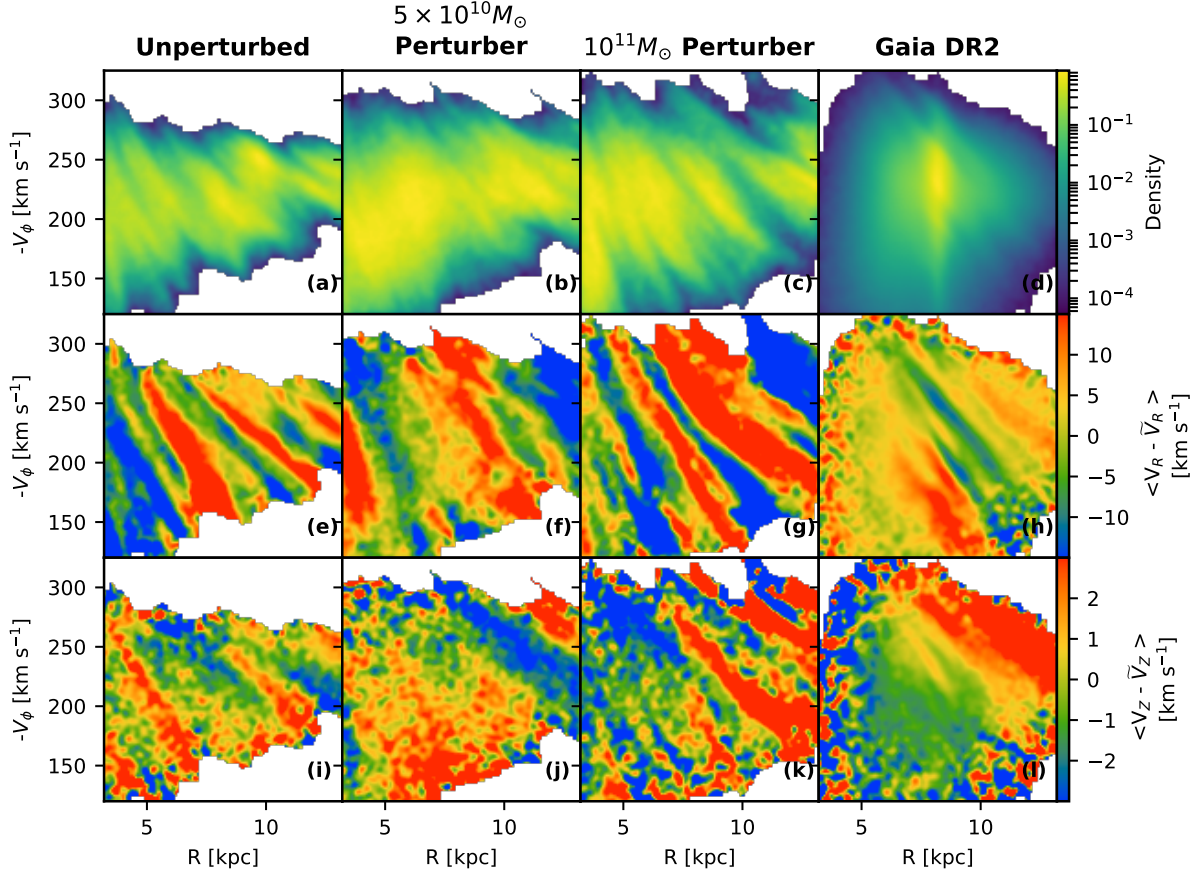
Figure 7. Comparison of features in the (R, V_ϕ) plane seen in N-body simulations with the observed data. Snapshots shown in panels(a-c) are at $\tau = 0.97$ Gyr, $\tau = 1.53$ Gyr, and $\tau = 1.54$ Gyr, respectively. In all panels, stars are selected in the region ($|R - R_\odot| < 5.0$)&($|\phi - \phi_\odot| < 25$).

both cases, Sgr crosses the disc at around $\tau = 0.15$ Gyr, and perturbs the galaxy from its equilibrium state. Previously, in simulations run in Bland-Hawthorn et al. (2019), we noted that disc crossing by Sgr wipes out previous coherent structure and generates new structures in the Galaxy. An evolution of $\tau = 1.5$ Gyr allows for enough time to develop, decay and phase mix the spiral arms as well as effects of Sgr.

For this reason we compare the unperturbed and perturbed scenarios at roughly coeval timestamps of ($\tau = 1.5$ Gyr), i.e., allowing for enough time for perturbations to phase mix.

Figure 7 shows the density, $\langle V_R \rangle$ and $\langle V_z \rangle$ maps in (R, V_ϕ) plane for the various N-body simulations alongside *Gaia DR*2. We note the presence of ridges in all three simulations (Figure 7(a,b,c)). Ridges are also present in the maps of $\langle V_R \rangle$ (Figure 7(f,g)) and $\langle V_z \rangle$ (Figure 7(j,k)).

In Figure 2, we saw that for *Gaia DR*2, ridges are correlated in kinematics and spatial density. In Figure 8 we explore similar correlations for our N-body simulations. We select stars around $(R, z, \phi) = (8.2, 0.0, 180.0°)$ and consider the profiles of $\langle V_z \rangle$, $\langle V_R \rangle$ and z against dimensionless orbital energy, $E' = (E - E_{circ}(R_\odot))/V_{circ}^2(R_\odot)$. For all simulations peaks can be seen in profiles of density, $\langle V_z \rangle$, z and V_R. It is worth noting that the unperturbed model has no tidal interactions, hence, the observed vertical oscillations for the unperturbed model must be due to internal processes.

A number of features seen in Figure 2 for the *Gaia DR*2 data

can also be seen in the simulations. The location of peaks in z match with location of peaks in v_z. Location of extrema in v_z match with location of peaks in density. For the the unperturbed case it is the minima that matches and for the high mass case it is the maxima. For the intermediate mass case we do not see such an association. We note that the matching of the location of peaks in z, v_z is not a general feature, as it was only seen at a few special locations within the galaxy.

The $\langle V_z \rangle$ profiles show a large scale trend like in the *Gaia DR*2 data. Such a trend is expected for the presence of a warp. A clear warp was detected in all our simulations, a plot of mean z and v_z as a function of ϕ showed a sinusoidal pattern with the v_z profile being shifted by 90° with respect to the z profile.

The amplitude of fluctuations for all the plotted quantities (density, $\langle V_z \rangle$, z and V_R), is considerably higher for the high mass Sgr case as compared to the other two simulations. A comparison with Figure 2 shows that the amplitude of $\langle V_z \rangle$, z and V_R fluctuations for the case of *Gaia DR*2 is comparable to the case of unperturbed and intermediate mass Sgr simulations, making the case of high mass perturber unfavourable.

3.4 Analysis of the (V_R, V_ϕ) plane: arches

We now study the (V_R, V_ϕ) plane. Figure 10 shows the distribution of *Gaia DR*2 stars. Arch like structures can be seen and they are asymmetrical about the $V_R = 0$ line. In Figure 9, we show the distri-
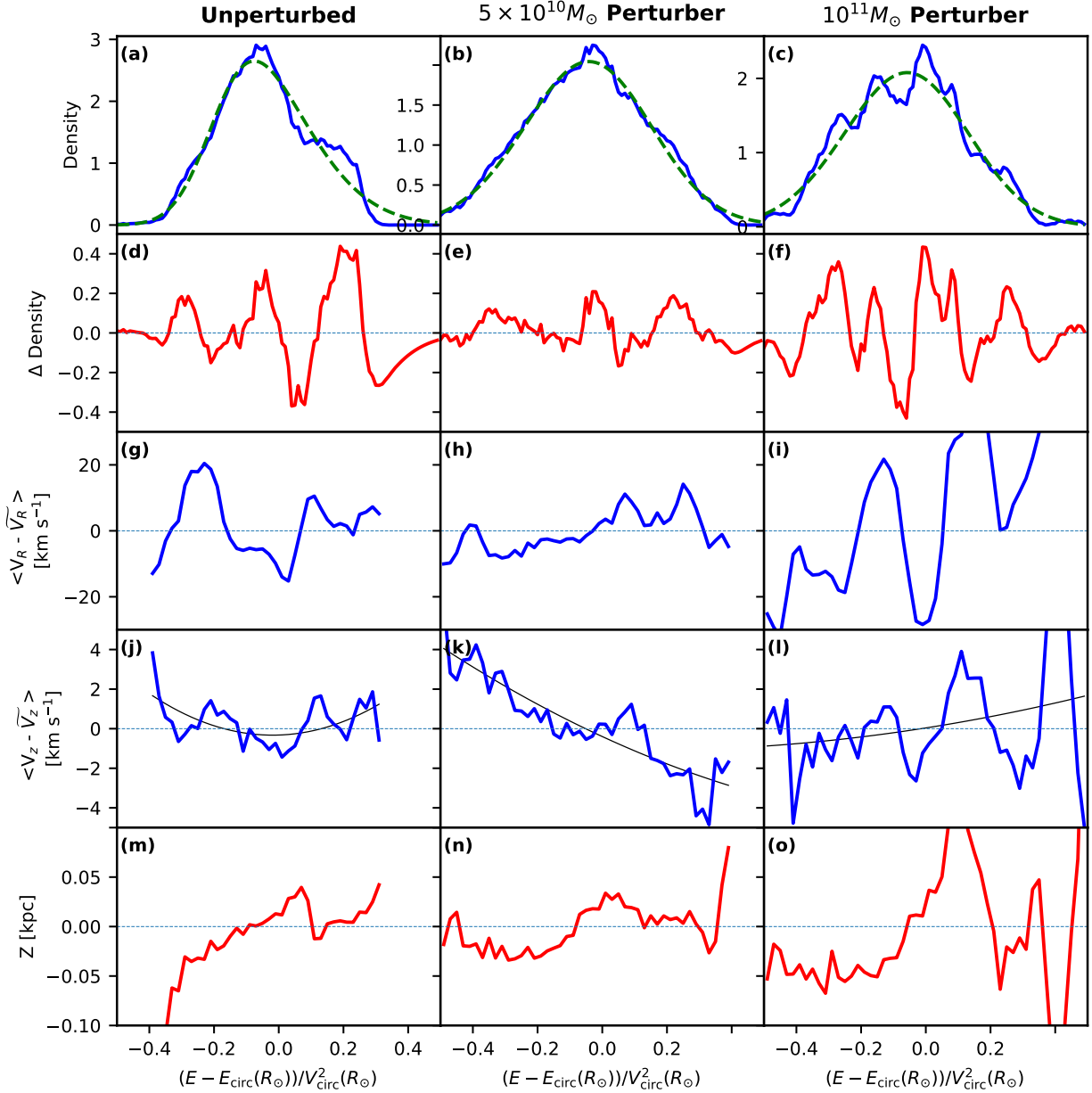
Figure 8. Profiles of different quantities as a function of orbital energy for stars in selected from disc N-body simulations. Results for galaxy that is unperturbed (Model P, left column panels), perturbed by inetermediate mass Sgr (Model S, middle column panels) and high mass Sgr (Model R, right column panels) are shown. Snapshots shown in panels(a-c) are at τ = 0.97 Gyr, τ = 1.53 Gyr, and τ = 1.54 Gyr, respectively. Panels(a-c) show the Energy distribution with a best fit skewed normal distribution (green dotted line). Panels(d-f) show the residuals in density distribution after subtracting the skewed normal. Panels(g-i) show the median vertical velocity, with a background fit for warp. Panels(j-l) show the vertical distance from the plane. Panels(m,o) show the median radial velocity profile. The figure is analogous to Figure 2.

bution of stars in the phase mixing simulation. Initially, there are no arches, but as time proceeds, arches start to appear, increase in number and become thinner. In the final snapshot, at 494 Myr, multiple arches are clearly visible, and they also appear to be asymmetrical as in the observed data.

We now study the distribution of stars in the (V_R, V_ϕ) space using disc N-body simulations. Figure 11 shows the distribution of stars for simulation P. We show snapshots corresponding to time τ of 250, 500, 1000 and 1500 Myr. For each time, we show distributions at four different locations in azimuth. The simulation starts with

a smooth disc and by 250 Myr strong tightly wound spiral arms can be seen, however the velocity distribution is devoid of any substructures at this stage. As the simulation evolves the velocity distribution becomes irregular and develops substructures. Arches are visible in all snapshots with τ >= 500 Myr and arches are not symmetric about the $V_R = 0$ line.

Figure 12 shows the distribution of stars for simulation S that corresponds to interaction with an intermediate mass satellite. Similarly Figure 13 shows the distribution for simulation R that corresponds to interaction with a high mass satellite. As compared
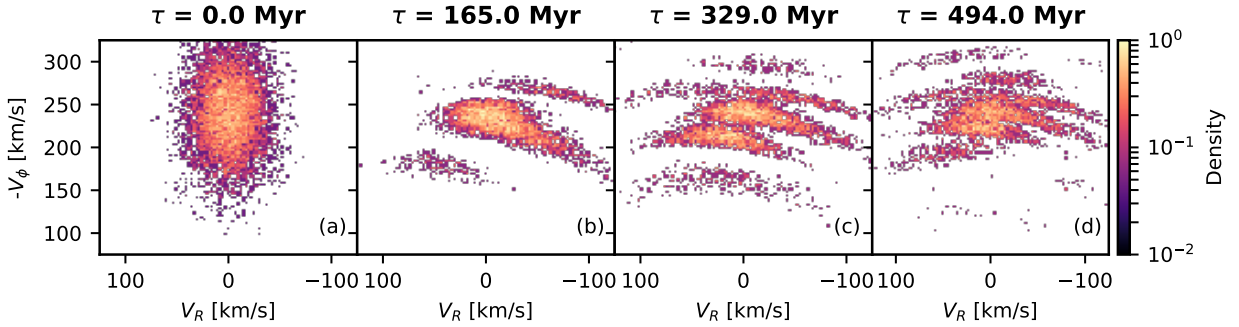
Figure 9. Evolution of stars in the phase mixing simulation (subsection 2.3), same as Figure 4, but here panels(a-d) show the (V_R, V_ϕ) plane. Stars are selected to lie in $(|\phi - 180.0°| < 25°)\&(|R - 8.2|/\text{kpc} < 0.25)$.

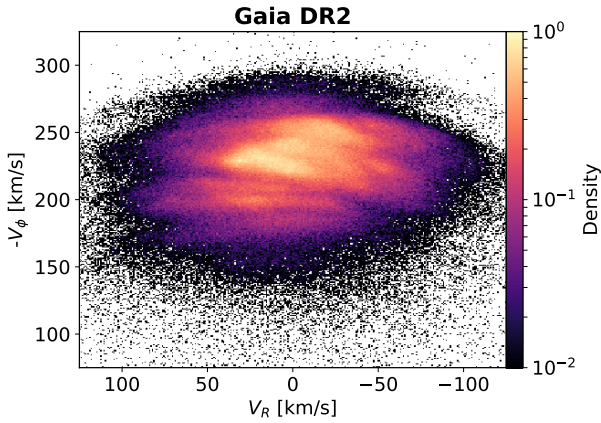**Figure 10.** Arches in the (V_R, V_ϕ) plane using *Gaia DR*2. Stars are selected to lie in $(|\phi - 180.0°| < 25°)\&(|R - 8.2|/\text{kpc} < 0.25)$.

4 DISCUSSION

We have explored the ridge like features in the (R, V_ϕ) plane using position and velocities from GAIA DR2 and elemental abundances from GALAH. We find that ridge like features are visible not only in the density maps but also in maps of $\langle V_R \rangle$, $\langle |z| \rangle$, $\langle V_z \rangle$, [Fe/H] and $[\alpha/\text{Fe}]$ (Figure 1 and Figure 3). The ridges are more prominent and visible to much larger ranges in R in the $\langle V_R \rangle$ map as compared to the density map. The $\langle |z| \rangle$ map suggests that the ridges are more prominent for stars close to the mid-plane of the Galaxy. The GALAH data suggests that ridges prefer stars with comparatively higher metallicity ($\sim$solar [Fe/H]) and solar $[\alpha/\text{Fe}]$ (Figure 3). Stars close to the plane have values of [Fe/H] and $[\alpha/\text{Fe}]$ that are close to solar. This explains the trends with elemental abundance. The preference for low $|z|$ could be due to one or all of the following three reasons: a) The ridges are due to transient perturbations (i.e., spiral arms) that are close to the plane and are disrupting and phase mixing with time; b) The ridges are due to interaction of stars with perturbations that are close to the plane; c) Stars close to the plane are kinematically cold and it is easier to perturb them.

Our phase mixing simulation of disrupting spiral arms can explain a wide array of kinematic features in the observed GAIA DR2 data. They simultaneously reproduce the ridges in (R, V_ϕ) plane, the ridges in the $\langle V_R \rangle$ maps (Figure 4), and the arches in (V_R, V_ϕ) plane (Figure 9). They also reproduce the observed asymmetry in the arches. While a perturbation from a bar has been shown to generate ridges, the number of ridges generated from a bar alone are too few to match the observed data (Antoja et al. 2018; Hunt et al. 2018). Phase mixing generates surfaces of constant energy and this explains the occurrence of both the ridges and the arches.

More realistic N-body simulations of a disc in which spiral arms are naturally generated support the results obtained from phase mixing. In these simulations the spiral arms grow in strength with time till about 500 Myr, and then start to decay. As the spiral arms decay and get phase mixed, the ridges and arches are found to grow in prominence, a phenomenon that was also seen in the phase-mixing simulation (Figure 6). Our N-body simulations also show ridges in the $\langle V_z \rangle$ maps as seen in the observed data. Simulations in which the disc is perturbed by the passage of an orbiting satellite also show features similar to that of an unperturbed disc (Figure 7). However, the ridges are found to be more pronounced in both the $\langle V_R \rangle$ and $\langle V_z \rangle$ maps due to the satellite passage.

Antoja et al. (2018) tentatively suggest that arches in the (V_R, V_ϕ) plane are projections of ridges in the (R, V_ϕ) plane. We note that, while ridges do suggest existence of discrete values of

to the simulation P of the unperturbed galaxy, considerably more substructures and arches can be seen in simulations S and R. The simulation R with high mass shows more arches than simulation S. It is clear that arches can develop even when there is no external perturber, but when a perturber like an orbiting satellite is present the arches are stronger and more numerous. The fact that the number and strength of arches depends upon the mass of the satellite, means that we can use the observed data to put limits on the satellite mass. From our set of simulations, we conclude that simulation P has too few arches and simulation R too many and it is the simulation S that matches best with the *Gaia DR*2 data.

3.5 Analysis of the (R, V_R) plane

Structures have been reported in the (R, V_ϕ) and (z, V_z) planes, but so far (V_R, R) space has not been explored. Figure A1 shows maps of density and $\langle V_\phi \rangle$ in the (V_R, R) phase space. The density map is extremely smooth and shows no substructures. However, arrow shaped substructures can be seen in the V_ϕ map. Phase mixing can explain the substructures seen in this space. Such substructures can also be seen in disc N-body simulations. These substructures provide additional independent constraints on models trying to explain the origin of phase space substructures in the Galaxy.
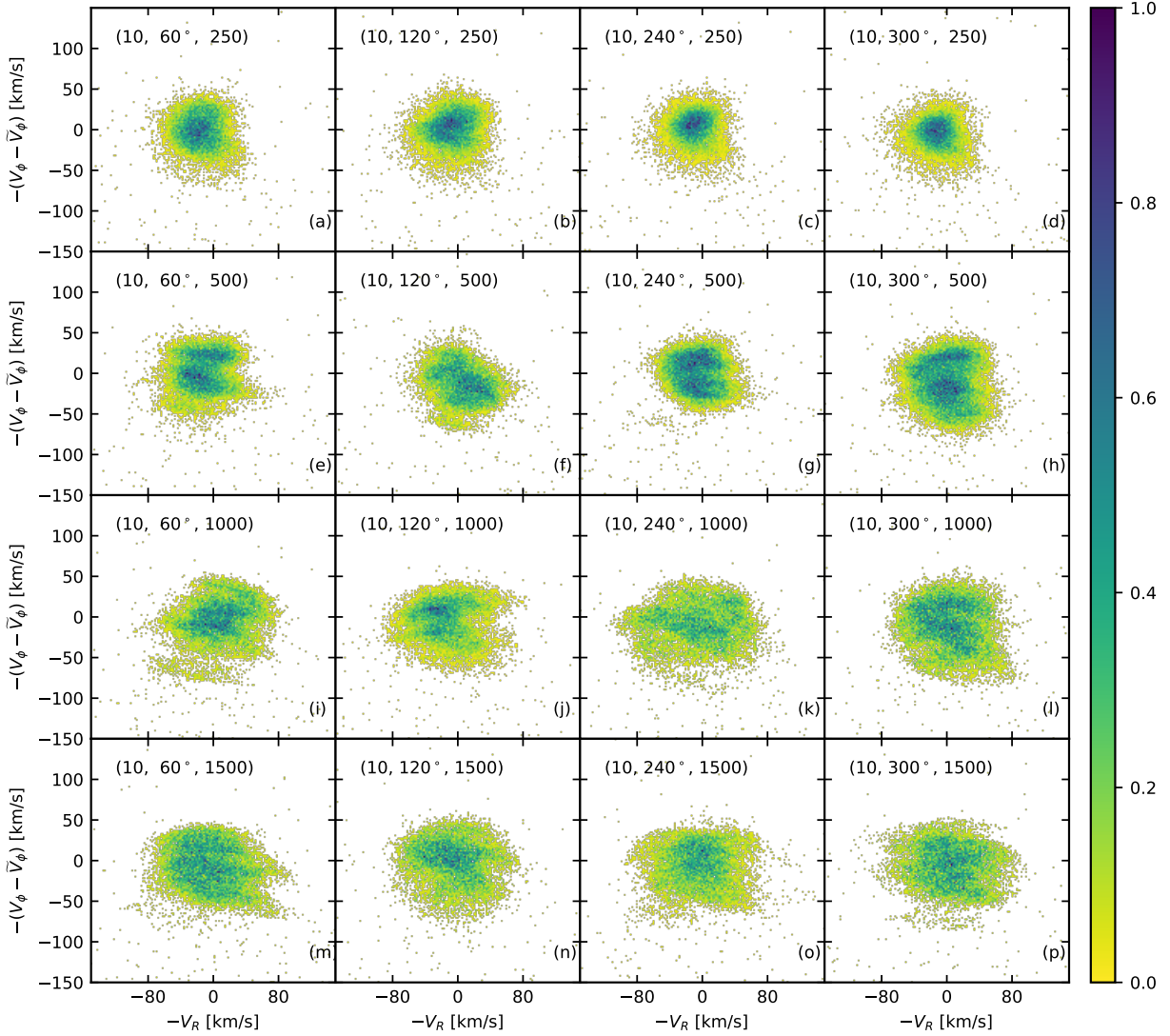
Figure 11. Distribution of stars in the (V_R, V_ϕ) plane for the N-body simulation P (Unperturbed Galaxy). Distributions for four different times and at various different azimuth angles are shown. The Galactocentric radius R, the azimuth angle ϕ and the time in Myr are labelled on the plots. Stars were restricted to $(|\Delta R| < 0.25\text{kpc})\&(|\Delta\phi| < 25°)$.

V_ϕ in the solar neighborhood, they do not necessarily suggest the presence of arches. It is impossible to deduce the distribution of V_R from the distribution of stars in (V_R, V_ϕ) plane. We have shown that phase mixing simulations of disrupting spiral arms not only generate ridges but also arches. The physical property unifying the two features is the energy. A ridge in (R, V_ϕ) and an arch in (V_R, V_ϕ) are both curves of constant energy. The phase mixing of disrupting spiral arms generates a regular pattern of peaks in the energy distribution of a sample confined to a narrow range in azimuth (Figure 4 o,p). A curve of constant energy and constant angular momentum both appear as a ridge in (R, V_ϕ) plane. However, only a constant energy curve will manifest itself as an arch in the (V_R, V_ϕ) plane.

The arches seen in Gaia DR2 are asymmetrical about the $V_R = 0$ line. We show that phase mixing simulations can generate asymmetrical arches, contradicting Quillen et al. (2018) who argue that phase mixing simulations cannot generate asymmetrical arches. However, the asymmetry is both apparent and intrinsic. The slight intrinsic asymmetry is due to the fact that an arch has a finite

width in energy and the V_R changes systematically with energy. This occurs in the initial stages when phase mixing is incomplete (Figure 9 b,c). The apparent asymmetry is due to the following reason and is responsible for asymmetry seen at later stages of phase mixing (Figure 9 d). The arch due to a single ridge and a single spiral arm is in general symmetrical in the (V_R, V_ϕ) plane, but the number density of stars is not symmetrical about V_R. Moreover, the arch is short and does not span the full range of V_R. When multiple arches from different spiral arms are superimposed they look like a large arch with a strong asymmetry.

We also see asymmetrical arches in N-body simulations in which a disc is evolved in a Milky Way like potential which includes a live dark matter halo (Figure 11). Asymmetrical arches were reported by Quillen et al. (2011) using similar simulations, but they did not study the effect of an interaction with a satellite. Laporte et al. (2018) studied simulations with an orbiting satellite and reported the presence of ridges but did not study the arches. We study simulations both with and without an orbiting satellite. We find that simulations
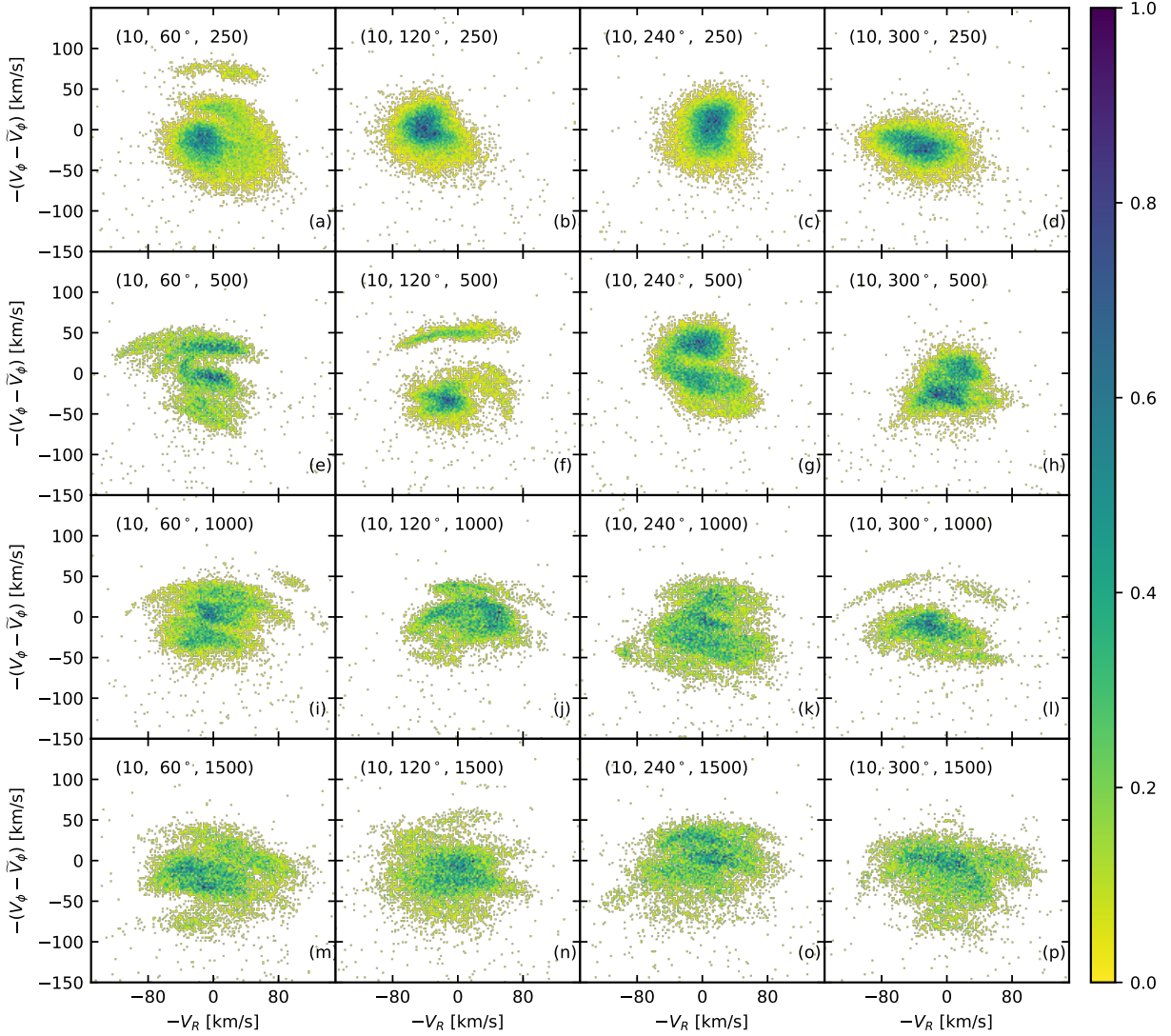
Figure 12. Analogue of Figure 11 but for stars in the N-body simulation S (interaction with an intermediate mass satellite).

in which the disc is perturbed by an orbiting satellite generates more arches. A high mass satellite generates more arches (Figure 13) than a satellite with lower mass (Figure 12). A $5 \times 10^{10} M_\odot$ satellite was found to describe the observed data the best. Arches develop within 250 Myr of interaction with a satellite, and are clearly visible even after 1 Gyr. Hunt et al. (2018), using backward integration of test particles in a winding spiral arm potential (Dehnen 2000), also reach a similar conclusion.

Antoja et al. (2018) used the V_ϕ separation of consecutive ridges and Minchev et al. (2009) used the V_ϕ separation of arches to conclude that the perturbation must be older than 1 Gyr and most likely about 2 Gyr. These conclusions are based on the assumption that the ridges are generated by a single perturber. If the ridges and arches are caused by more than one transient spiral arms, then each arm will have its own set of ridges and the separation between the ridges can be smaller as compared to the case of a single perturber for any given age of the perturber. Hence, the V_ϕ separation cannot be used to reliably date the perturber.

One of the most interesting result of our study is the existence of ridges in $\langle V_z \rangle(R, V_\phi)$ map (Figure 1c). At a given R when $\langle V_z \rangle$ is

plotted as function of angular momentum or energy the ridges show up as undulations with clearly defined peaks and valleys (Figure 2). In addition to undulations, a smooth large scale trend is also seen, the V_z increases with L for $L/(V_{\rm circ}(R_\odot)R_\odot) > 1$. This rise of V_z has been associated with the onset of the warp (Poggio et al. 2017; Schönrich & Dehnen 2018; Poggio et al. 2018). However, the origin of the undulations is not clear. The data shows that the locations of at least two and possibly three V_z peaks coincide with the density peaks. This can be interpreted as ridges having a net upward motion. Undulations are also seen in profiles of z with energy. Three peaks are clearly identifiable in z and they match with peaks in V_z.

A 3D phase mixing simulation with an initial dispersion of 10 km s^{-1} in V_z was unable to reproduce the ridges in $\langle V_z \rangle(R, V_\phi)$ map. This suggests that the origin of features in V_z is dynamical with the self gravity of the disc playing a role. The simulations of both the unperturbed disc and the disc perturbed by a massive satellite shows ridges in $\langle V_z \rangle(R, V_\phi)$ map (Figure 7). For the two cases of the perturbed disc the profile of z as a function of orbital energy is also found to show undulations (Figure 8). For the case of the high mass perturber the most prominent peak in V_z shows a clear match
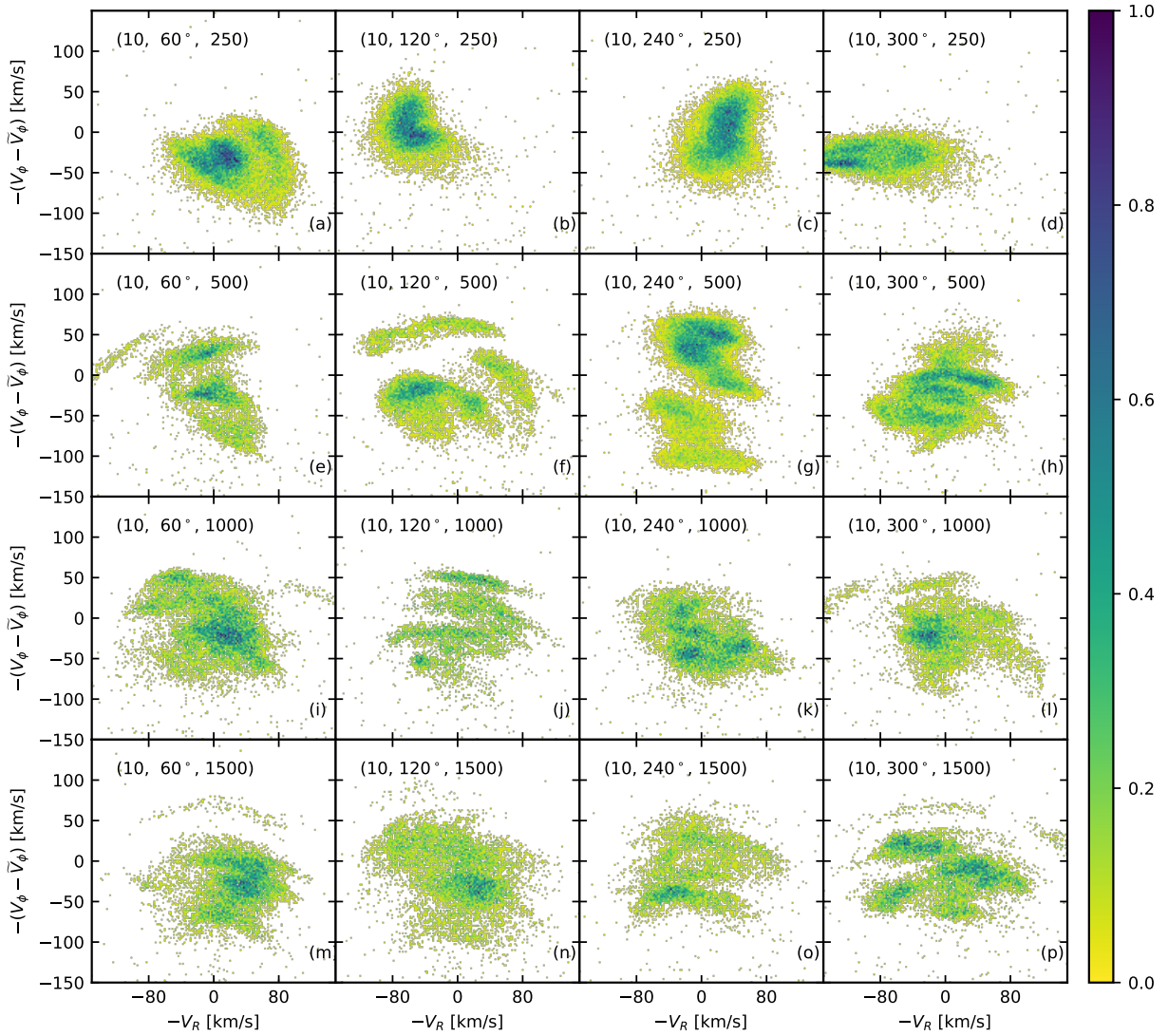
Figure 13. Analogue of Figure 11 but for stars in the N-body simulation R (interaction with a high mass satellite).

with the most prominent peak in z. While an interaction with an orbiting satellite can easily couple planar and vertical motions, e.g. they are known to generate warps, the case of an unperturbed disc generating such a coupling is intriguing. However, Masset & Tagger (1997) have shown that non-linear coupling between the spiral wave of the galaxy and the warp waves can lead to warps in isolated disc galaxies.

Another example of coupling between the vertical and planar motion is the existence of the spiral pattern in the (z, V_z) plane (Antoja et al. 2018). This spiral pattern is seen in density maps, $\langle V_R \rangle$ maps and $\langle V_\phi \rangle$ maps. It has been shown that such a coupling can be generated by the impact of a satellite passing through the disc (Bland-Hawthorn et al. 2019; Laporte et al. 2018; Binney & Schönrich 2018), or due to the buckling of the bar (Khoperskov et al. 2018). So far there has been nothing that suggests any link between the ridges and the (z, V_z) plane spiral.

We note that the average z or V_z integrated over a single (z, V_z) phase space spiral is non zero and depends upon the orientation of the spiral. So if the orientation of the spiral changes with L_z, we can expect a change of $\langle V_z \rangle$ with L_z. We find that the L_z as

compared to V_ϕ is a more robust quantity to characterize the phase space spiral. This is because the spiral pattern for a given L_z (or orbital energy) is almost invariant with the Galactocentric radius R (also with azimuth ϕ), in a distance of around 1 kpc around the Sun, but V_ϕ is not. When the (z, V_z) plane is studied for different values of L_z, we find that the spiral pattern is present for a wide range of L_z and the orientation of the spiral changes with L_z. However, the density distribution along the spiral is not constant and this can override any signatures in $\langle V_z \rangle$ generated by the spiral. Therefore, at this stage it is difficult to establish any link between the phase space spiral and the ridges or the warp.

vided by national institutions, in particular the institutions participating in the *Gaia* Multilateral Agreement.

The GALAH survey is based on observations made at the Australian Astronomical Observatory, under programmes A/2013B/13, A/2014A/25, A/2015A/19, A/2017A/18. We acknowledge the traditional owners of the land on which the AAT stands, the Gamilaraay people, and pay our respects to elders past and present. Parts of this research were conducted by the Australian Research Council Centre of Excellence for All Sky Astrophysics in 3 Dimensions (ASTRO 3D), through project number CE170100013.

This research has made use of Astropy13, a community-developed core Python package for Astronomy (Astropy Collaboration et al., 2013). This research has made use of NumPy (Walt et al., 2011), SciPy, and MatPlotLib (Hunter, 2007).

REFERENCES

Antoja T., et al., 2014, A&A, 563, A60
Antoja T., et al., 2018, Nature, 561, 360
Bennett M., Bovy J., 2019, MNRAS, 482, 1417
Bensby T., Feltzing S., Oey M. S., 2014, A&A, 562, A71
Binney J., Schönrich R., 2018, MNRAS, 481, 1501
Bland-Hawthorn J., Gerhard O., 2016, ARA&A, 54, 529
Bland-Hawthorn J., et al., 2019, MNRAS
Bovy J., 2015, ApJS, 216, 29
Buder S., et al., 2018, MNRAS, 478, 4513
D'Onghia E., Madau P., Vera-Ciro C., Quillen A., Hernquist L., 2016, ApJ, 823, 4
Dehnen W., 2000, AJ, 119, 800
Duong L., et al., 2018, preprint, (arXiv:1801.01514)
Fragkoudi F., et al., 2019, arXiv e-prints, p. arXiv:1901.07568
Gaia Collaboration et al., 2018a, A&A, 616, A1
Gaia Collaboration et al., 2018b, A&A, 616, A11
Gómez F. A., Minchev I., O'Shea B. W., Beers T. C., Bullock J. S., Purcell C. W., 2013, MNRAS, 429, 159
Gravity Collaboration et al., 2018, A&A, 615, L15
Hattori K., Gouda N., Tagawa H., Sakai N., Yano T., Baba J., Kumamoto J., 2019, MNRAS, 484, 4540
Hayden M. R., et al., 2014, AJ, 147, 116
Hernquist L., 1990, ApJ, 356, 359
Huang Y., et al., 2018, ApJ, 864, 129
Hunt J. A. S., Bovy J., 2018, MNRAS, 477, 3945
Hunt J. A. S., Hong J., Bovy J., Kawata D., Grand R. J. J., 2018, MNRAS, 481, 3794
Kawata D., Baba J., Ciucă I., Cropper M., Grand R. J. J., Hunt J. A. S., Seabroke G., 2018, MNRAS, 479, L108
Kazantzidis S., Magorrian J., Moore B., 2004, ApJ, 601, 37
Khoperskov S., Di Matteo P., Gerhard O., Katz D., Haywood M., Combes F., Berczik P., Gomez A., 2018, arXiv e-prints, p. arXiv:1811.09205
Laporte C. F. P., Minchev I., Johnston K. V., Gómez F. A., 2018, arXiv e-prints, p. arXiv:1808.00451
Mackereth J. T., et al., 2017, MNRAS, 471, 3057
Malhan K., Ibata R. A., Martin N. F., 2018, MNRAS, 481, 3442
Masset F., Tagger M., 1997, A&A, 318, 747
Minchev I., Quillen A. C., Williams M., Freeman K. C., Nordhaus J., Siebert A., Bienaymé O., 2009, MNRAS, 396, L56
Miyamoto M., Nagai R., 1975, PASJ, 27, 533
Monari G., Famaey B., Fouvry J.-B., Binney J., 2017, MNRAS, 471, 4314
Niederste-Ostholt M., Belokurov V., Evans N. W., PeÃśarrubia J., 2010, ApJ, 712, 516
Nieva M.-F., Przybilla N., 2012, A&A, 539, A143
Pérez-Villegas A., Portail M., Wegg C., Gerhard O., 2017, ApJ, 840, L2
Perret V., Renaud F., Epinat B., Amram P., Bournaud F., Contini T., Teyssier R., Lambert J.-C., 2014, A&A, 562, A1
Perryman M. A. C., et al., 1997, A&A, 323, L49

Poggio E., Drimmel R., Smart R. L., Spagna A., Lattanzi M. G., 2017, A&A, 601, A115
Poggio E., et al., 2018, MNRAS, 481, L21
Price-Whelan A. M., Bonaca A., 2018, ApJ, 863, L20
Quillen A. C., Dougherty J., Bagley M. B., Minchev I., Comparetta J., 2011, MNRAS, 417, 762
Quillen A. C., et al., 2018, MNRAS, 480, 3132
Ramos P., Antoja T., Figueras F., 2018, A&A, 619, A72
Reid M. J., Brunthaler A., 2004, ApJ, 616, 872
Schönrich R., Dehnen W., 2018, MNRAS, 478, 3809
Schönrich R., Binney J., Dehnen W., 2010, MNRAS, 403, 1829
Sellwood J. A., 2011, MNRAS, 410, 1637
Sellwood J. A., 2012, ApJ, 751, 44
Sharma S., et al., 2018, MNRAS, 473, 2004
Soubiran C., et al., 2018, A&A, 616, A7
Springel V., Di Matteo T., Hernquist L., 2005, MNRAS, 361, 776
Tepper-García T., Bland-Hawthorn J., 2018, MNRAS, 478, 5263
Teyssier R., 2002, A&A, 385, 337
Trick W. H., Coronado J., Rix H.-W., 2018, preprint, p. arXiv:1805.03653 (arXiv:1805.03653)
Wittenmyer R. A., et al., 2018, AJ, 155, 84
Zwitter T., et al., 2018, MNRAS, 481, 645

APPENDIX A: GAIA SQL QUERY

```
Select * from gaiadr2.gaia_source G
where G.parallax IS NOT Null
AND G.parallax_error/G.parallax < 0.2
AND G.parallax > 0.\
where G.radial_velocity IS NOT Null
```

This paper has been typeset from a T$_{\rm E}$X/L$^{\rm A}$T$_{\rm E}$X file prepared by the author.
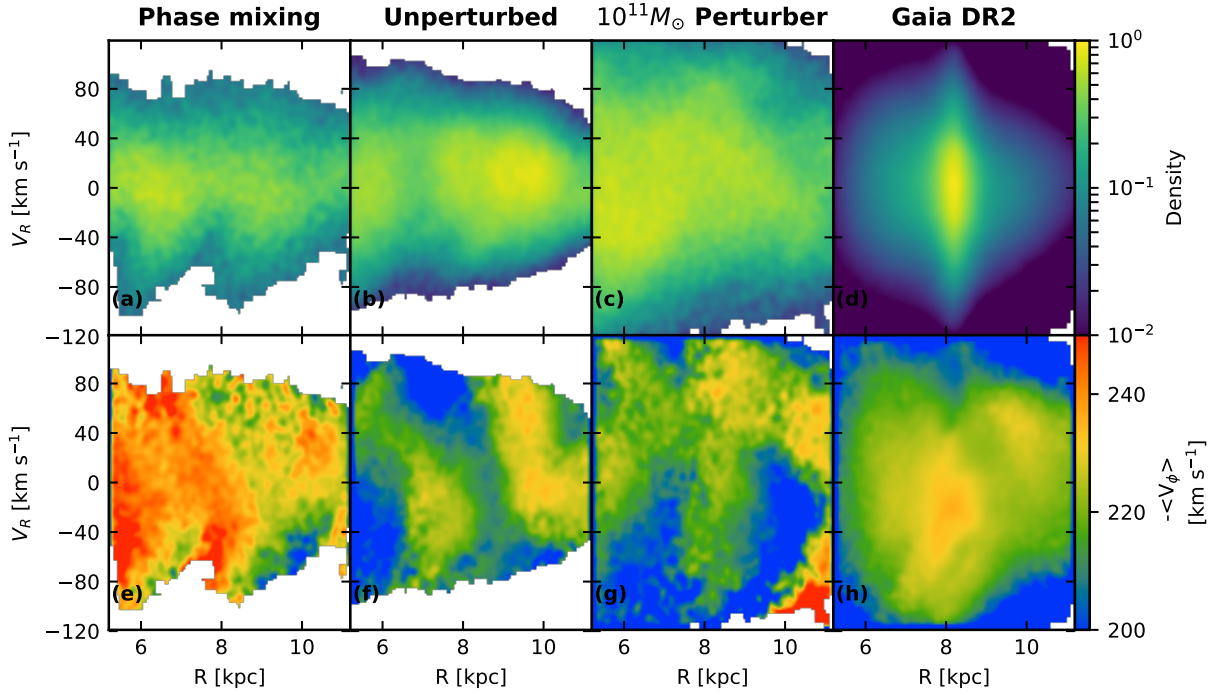
Figure A1. Maps of density and $\langle V_\phi \rangle$ in the (R, V_R) space. (a,e) Phase mixing simulation ($\tau = 494$ Myr). (b,f) Simulation of an unperturbed disc ($\tau = 0.97$ Gyr). (c,g) Simulation of a disc perturbed by a high mass satellite ($\tau = 1.54$ Gyr) (d,h) Gaia DR2. The density maps are smooth, but the $\langle V_\phi \rangle$ maps show cone like structures (similar to a rotated pine tree), which are also predicted by phase mixing simulations.
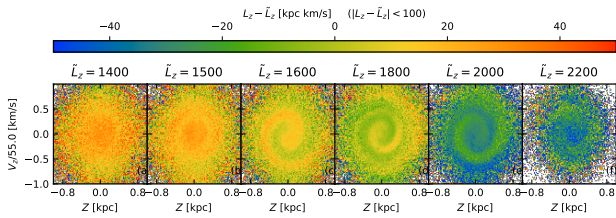

Figure A2. The distribution of stars in the (z, V_z) plane for 200 kpc km s^{-1} wide slices in angular momentum L_z. The overall median L_z for each slice is labelled on the top. The image shows a map of median residual angular momentum in each pixel. The spiral pattern is visible for a wide range of angular momentum and the orientation of the spiral is found to change with L_z.
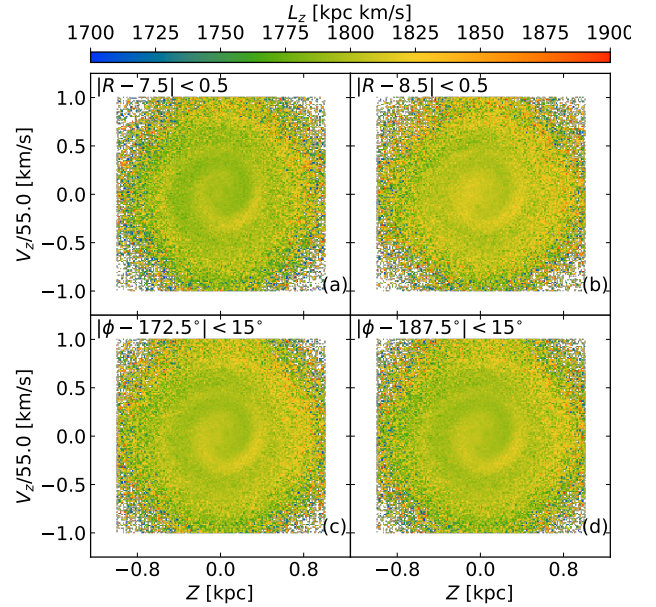

Figure A3. Map of median $\langle L_z \rangle$ in the (z, V_z) plane for various different Galactic positions. The orientation of the spiral